THE JOURNAL OF PHYSICAL CHEMISTRY C
A JOURNAL OF THE AMERICAN CHEMICAL SOCIETY

pubs.acs.org/JPCC

Article

Distinguishing the Roles of Atomic-Scale Surface Structure and Chemical Composition in Electron Phonon Coupling of the Nb(100) Surface Oxide Reconstruction

Published as part of The Journal of Physical Chemistry C virtual special issue "Alec Wodtke Festschrift".

Caleb J. Thompson, Michael Van Duinen, Cristobal Mendez, Sarah A. Willson, Van Do, Tomás A. Arias, and S. J. Sibener*

Cite This: *J. Phys. Chem. C* 2024, 128, 10714−10722

Read Online

ACCESS | Metrics & More | Article Recommendations

ABSTRACT: The (3 × 1)-O/Nb(100) surface λ_S was measured to be 0.20 ± 0.06, and its atomic-scale surface structure was confirmed. These results were supported by consistency between measured helium atom scattering Debye−Waller factors and *ab initio* density-functional theory predictions. The λ_S measured for the (3 × 1)-O surface reconstruction is further diminished from the metallic, unreconstructed Nb(100) value and the reported bulk Nb λ values. Furthermore, varying subsurface O has no significant effect on the λ_S of the (3 × 1)-O reconstruction. While the metallic, unreconstructed Nb(100) surface is significantly affected by accumulated subsurface C and O, the (3 × 1)-O reconstruction stabilizes its λ_S against the effects of subsurface O. Due to the low λ_S, a negligible critical temperature $(T_C) \leq 6.2 \times 10^{-3}$ K was estimated, indicating that at operational temperatures of ∼2 K, the (3 × 1)-O/Nb(100) reconstruction is not superconducting alone. However, the proximity effect indicates that a thin normal metal in contact with a superconductor exhibits some superconducting properties while the superconductor's properties are diminished. These results contain the first measurement of (3 × 1)-O/Nb(100) λ_S, distinguish the effects of surface structure and chemical composition on λ_S, and indicate that the (3 × 1)-O/Nb(100) surface has diminished superconducting properties relative to the unreconstructed, metallic Nb(100) and the Nb bulk.

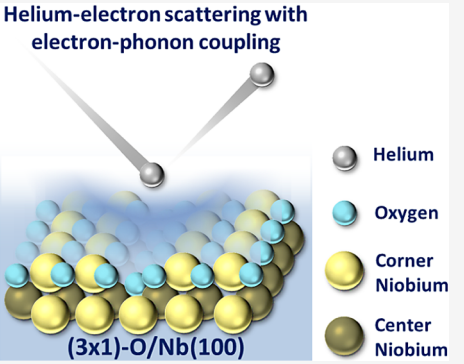

1. INTRODUCTION

Niobium is the standard material for superconducting radio frequency cavities in high-energy particle accelerators. Nb found its ubiquitous use and extensive study in SRF cavities due to both its normal and superconducting state properties.[1−4] For example, Nb's relatively high ductility enables facile shaping of optimal cavity geometries for relatively high quality (Q) factors and accelerating fields.[1,2,5] Additionally, pure Nb has a relatively high thermal conductivity facilitating sufficient cooling, essential to enter and maintain Nb's superconducting state.[2,3] Nb's superconducting state's relatively high critical temperature (T_C) and low RF surface resistance (R_s) drive high Q factors at attainable operating temperatures.[2,4] The superconducting state's capability of repelling magnetic fields contains accelerating RF fields. In fact, the RF field only penetrates up to ∼100 nm in Nb SRF cavities, thus RF field energy losses occur along the SRF cavity's surface.[2,6] The Nb's SRF cavity's RF surface resistance determines the magnitudes of the energy losses.[2,7] These losses heat the SRF cavity, in turn requiring more cooling to maintain the optimal operational temperatures and driving up costs of operation.[8,9] Experimental and theoretical studies have documented and studied mechanisms in which even local hot spots from inhomogeneities, defects, and topographical variations can heat and quench entire SRF cavities.[5,9−14] Thus, optimal preparation of Nb SRF cavity surfaces is required to prepare energetically efficient SRF cavities and keep costs of operation from being prohibitively high. In other words, the relationship between the atomic-scale surface structure and the resulting superconducting properties at the surface is critical in improving and developing next generation SRF cavity materials.

Extensive study of Nb and Nb SRF cavities has pushed their performance to the fundamental limits of operation. Thus, the SRF community has begun developing new materials and cavity treatments to further reduce R_s, maximize the superheating field (H_{sh}), minimize power loss, and optimize overall

Received: April 14, 2024
Revised: May 24, 2024
Accepted: May 30, 2024
Published: June 11, 2024

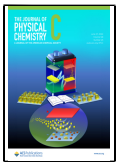

Downloaded via UNIV OF CHICAGO on August 1, 2024 at 21:21:59 (UTC).
See https://pubs.acs.org/sharingguidelines for options on how to legitimately share published articles.

ACS Publications
© 2024 American Chemical Society

performance.[5,10,15−17] In fact, defects, inhomogeneities, and impurities at the surfaces limit cavity quality factors and operating temperatures, limiting the implementation of promising new SRF cavity materials.[4,5,11,12,15,18,19] While well-studied, the formation and evolution of surface defects and compositional inhomogeneities remain a challenging part of SRF cavity treatment design and implementation. Such an understanding of the role of surface structure and chemical composition, as well as their resulting effects on superconductivity at the surface, remains elusive. This relationship is not well understood, and we have only just begun its elucidation with simultaneous *in situ* atomic scale surface structure and surface EPC measurements on the bare metallic Nb(100) surface.[20]

Conventional superconducting states form due to electron−phonon interactions that condense electrons into Cooper pairs.[7,21−24] The electron−phonon coupling (EPC) constant (λ) is a dimensionless constant that quantifies the effective strength of electron−phonon interactions in a material.[24,25] Furthermore, this constant determines many superconducting properties such as the critical temperature (T_C) and superconducting gap.[7,24,25] We have brought into effective action helium (He) atom scattering's (HAS) sensitivity to both *in situ* high-temperature surface structure and surface EPC (SEPC) constant (λ_S) to connect atomic-scale surface structure with its effect on λ_S and thus surface superconductivity. Previously, we have demonstrated this capability by measuring λ_S and atomic-scale surface structure simultaneously on the unreconstructed Nb(100) surface and now set forth in this work the results of a similar study on the Nb(100) surface oxide reconstruction.[20]

Due to Nb's exceptional affinity for O and spontaneous O surface segregation, Nb surfaces exposed to air are reconstructed by a robust and complex oxide.[26−28] The Nb surface oxide system has been studied extensively with a variety of techniques and requires prohibitively high temperatures (<2400 K) to remove O as sublimed NbO.[26−34] Upon exposure to air at ambient conditions, a ∼ 5 nm pentoxide film spontaneously forms.[28,33] It has been shown through XPS that for both single crystal and polycrystalline Nb surfaces, the pentoxide film dissolves above 600 K in UHV conditions, forming a monolayer of NbO.[26,29,34] These conditions match those typical of Nb SRF cavity preparations, and we expect the Nb surface to form the thermodynamic minimum of the system, a NbO monolayer. On the Nb(100) face, the NbO monolayer's most stable phase is the (3 × 1)-O superlattice reconstruction. In fact, this surface oxide reconstruction has been demonstrated with *in situ* high temperature helium diffraction and high temperature AES to be stable up to 1130 K in terms of structure, order, and composition.[35] In other words, the Nb(100) face under typical SRF cavity preparations (both those treating the native Nb surface and those that grow new materials on it) forms a stable NbO surface reconstruction. Furthermore, the synergy of HAS time-of-flight measurements and novel DFT calculations found that exceptionally strong Nb−Nb and Nb−O bonds make up the (3 × 1)-O ladder protrusions, exhibiting forces significantly larger in magnitude than any forces in the bulk Nb and unreconstructed Nb(100) surface. In other words, these atomic-scale ladder protrusions were identified as a key driving force for the (3 × 1)-O reconstruction's stability and are a significant barrier to incorporation or alloying of SRF cavity treatments.

While we have recently made the first measurement of surface EPC on any Nb surface, specifically the metallic, unreconstructed Nb(100) surface, EPC in bulk Nb has been studied thoroughly.[36−45] The λ of bulk Nb has been measured by electronic Raman scattering (1.15),[41] proximity electron tunneling spectroscopy (1.04 ± 0.06),[45,46] femtosecond pump−probe measurements (1.16 ± 0.11),[43] and calculated with McMillan's expression for T_C from accompanying measurements of appropriate normal-state parameters (0.92).[38] Recently, we measured the EPC of the bare metal surface to be 0.50 and used it to estimate benchmark superconducting properties, correlating atomic scale structure to speculative SRF cavity performance.[20] The diminished EPC at the surface of the unreconstructed metallic Nb(100) surface implies that even without O or reconstruction, the presence of an interface approximately halves the λ. However, as established in the literature, the state of a Nb(100) surface under SRF cavity preparation conditions readily forms the (3 × 1)-O surface oxide reconstruction on the Nb(100) face.[26,29,34,35] The effects of interstitial O on bulk Nb superconductivity have been investigated.[38,39] Note that interstitial octahedral O dissolved in the Nb lattice is distinct from an oxide reconstruction that forms a superlattice. DeSorbo reports[38] that below the solubility limit interstitial O atoms decrease T_C by 0.93 K per at. % O while Koch et al. report[39] that increasing amounts of interstitial O not only decrease T_C, but also decrease the electronic coefficient of low-temperature-specific-heat capacity, electronic density of states at the Fermi level, and λ. Thus, notably O impacts bulk Nb's EPC via not just the phonons of Nb, but also via the electronic states.[39]

While the measurement of the bare metal λ yields new insight, this result cannot distinguish the effect of the interface from that of the surface oxide reconstruction on the surface superconductivity. Thus, there remains a critical gap in the foundational knowledge of the atomic scale surface structure and composition as well as its effects on SRF cavity performance. An important part of that gap is the correlation of structure and composition of the NbO surface oxide monolayer to the resulting surface superconducting properties.

Supersonic helium beams have been used to probe surfaces since the 1920s. Their lack of penetration into the bulk, chemical inertness, and remarkably narrow velocity distributions are sufficient to create a truly surface sensitive technique.[47−49] The de Broglie wavelength and narrow momentum distribution of He atoms are well matched to atomic-scale structure and allow for precise measurements.[50,51] Coincidentally, the momentum and energy of He atoms sufficiently resonate with surface phonons, making HAS uniquely suited to measure and resolve low-energy phonon modes at surfaces.[47,51−53] While helium atoms exchange energy with phonons, the helium atoms scatter off of the electron density.[54] Thus, inelastic helium−phonon scattering events are actually two concerted scattering events: helium−electron and electron−phonon. A theoretical description of this helium−electron−phonon scattering event has been developed for metals, semiconductors, topological insulators, 2D materials, and metallic films to show that the Debye−Waller (DW) factor is directly proportional to the SEPC (λ_S).[51,55−64] The derivation starts from the distorted-wave Born approximation, using second-order perturbation theory to define electron−phonon matrix elements, and adopting additional yet reasonable approximations.[55,56] The DW factor

https://doi.org/10.1021/acs.jpcc.4c02430
J. Phys. Chem. C 2024, 128, 10714−10722

describes thermal attenuation of the scattered He intensity and does so as a multiplicative factor present in all scattering probabilities.[47,51] This DW factor originally came from neutron and X-ray scattering, accounting for motion of nuclei in the lattice from thermal excitation of phonons.[23,47,50] However, after being applied to helium atom scattering, the theory was developed and the role of the electron density elucidated.[51,57] Simply put, the thermal excitation of phonons at or near enough to the surface perturbs the surface electron density, reducing the coherence of the scattered He and measured HAS intensity.[51,55−57]

The work presented herein provides the first measurement of λ of the (3 × 1)-O/Nb(100) surface oxide reconstruction. These results distinguish the effect of the surface oxide reconstruction from that of interstitial oxygen on Nb(100)'s surface superconductivity.[20] These findings begin to fill a critical gap in the foundational knowledge of the effect of atomic scale surface structure and composition on SRF cavity performance.

2. METHODS

2.1. Experiment. Measurements and surface preparations were performed with a UHV scattering instrument. The instrument has been detailed elsewhere, but is summarized here.[35,53,65,66] The scattering instrument consisted of three main sections: a differentially pumped beam source, a sample chamber, and a differentially pumped rotating detector. The sample surface was prepared and HAS, AES, and LEED measurements made *in situ* within the sample chamber. A supersonic atomic or molecular beam was created by expansion from a 15 μm nozzle that was cooled with a closed-cycle He refrigerator. A skimmer extracted the supersonic beam from within the expansion, allowing the extracted portion of the expansion to continue into the second differentially pumped chamber. In the second differentially pumped chamber, the beam was pulsed with a mechanical chopper. The resulting supersonic beam was nearly monoenergetic ($\Delta v/v \leq 1\%$), making a ∼4 mm beam spot size on a 1 cm sample, scattering into 2π steradians. A triply differentially pumped, computer-controlled, rotatable detector arm collected scattered atoms or molecules with angular and temporal resolution. Once inside the detector, the probe atoms or molecules were ionized by electron bombardment between the differentially pumped detector regions, then mass selected using a quadrupole mass spectrometer, and detected with an electron multiplier, followed by pulse counting electronics. The flight path was 1.5277 m, the sum of the chopper-to-sample path was 0.4996 m, and the sample to ionizer path was 1.0281 m. For our experiments, we used a helium supersonic beam to probe the Nb(100) surface.

Diffraction scans were obtained by square-wave beam modulation, with a 50% duty cycle and rotating the detector at 0.2° increments with fixed incident angle and energy, with an overall instrument angular resolution of 0.20°. The beam was characterized by time-of-flight (TOF) measurements made with a single-slit chopping, 1% duty cycle pattern. The Nb(100) crystal was mounted on a six-axis manipulator within the HAS instrument's sample chamber. This manipulator enables control over the incident angle, θ_i, azimuthal angle, ϕ, and tilt, χ, with respect to the scattering plane. Electron bombardment heating and a closed-cycle He refrigerator modulated the sample temperature within a range of 300 to 2300 K. Surface Preparation Laboratory (The Netherlands) provided the Nb(100) sample (99.99% purity, ∼ 0.1° cut accuracy), which we then cleaned in the HAS instrument by cycles of annealing and flashing up to 1900 K, in addition to sputtering with 1 keV Ne^+ ions (3 μA maximum) and exposing to backfilled O at a surface temperature (T_S) of ∼1200 K to remove surface C as desorbed CO. These temperatures were measured with a pyrometer. Impurities identified by *in situ* AES were C, B, S, and N; these were removed by the combination of annealing, flashing, sputtering, and 1200 K T_S exposure to O. We continued the cleaning cycles until only Nb and O were present on the surface in the appropriate ratio, as confirmed by AES, and until the surface was smooth enough for high-intensity He diffraction. Due to the annealing, flashing, sputtering and O exposure process described above, the surface oxide reconstructed (3 × 1)-O/Nb(100) surface formed naturally and spontaneously. The (3 × 1)-O/Nb(100) surface structure and cleanliness was confirmed with AES, LEED, and helium diffraction. During data collection, the Nb sample was periodically flashed to about 1200 K to eliminate unwanted surface adsorbates. Debye−Waller data were obtained by aligning the crystal at each surface temperature and taking diffraction scans across the specular peak. Each Debye−Waller measurement consisted of varying surface temperature up and then down a chosen temperature range, aligning the crystal and taking diffraction scan over specular at each temperature. These measurements were taken from the lower limit, ∼550 K, of the chosen temperature range to the upper limit, ∼750 K, then immediately back down to the lower limit. The lower temperature limit was determined as the lowest temperature free of substantial background gas adsorption in the time it took to align and take a diffraction scan. The temperature during the Debye−Waller measurement heating the crystal was measured with a type K thermocouple attached to the plate holding the crystal.

The work function of the (3 × 1)-O/Nb(100) surface oxide reconstruction was calculated from ultraviolet photoelectron spectroscopy (UPS) measurements taken in a separate UHV chamber. The (3 × 1)-O structure was formed on a second Nb(100) single crystal, and the surface cleanliness was confirmed with AES. The UPS measurements were collected using a helium discharge lamp (Specs UVS 10/35) optimized for He I photon emission (21.22 eV) positioned 45° above the sample plane. The photoemission spectra were collected by using a cylindrical mirror analyzer (Staib DESA 100). The low kinetic energy portion of the UPS spectrum was obtained by applying a negative voltage to the Nb(100) sample with an external DC source (Agilent E3612A).

2.2. Theoretical Background. To study the (3 × 1)-O/Nb(100) surface, we performed density-functional theory (DFT) calculations using open-source planewave software JDFTx.[67,68] We implemented ultrasoft pseudopotentials,[69] using an effective temperature of 20 milli-Hartree and a Fermi function to determine electronic occupancies. The exchange-correlation energy was approximated using the Perdew−Burke−Ernzerhof functional (PBE).[70] Our calculations employed planewave cutoff energies of 20 and 100 hartree for the electronic wave functions and density, respectively. We computed properties of a slab with six layers of niobium atoms and two layers of oxygen atoms along the surface-normal direction and truncated Coulomb potentials to increase the accuracy of calculated surface properties.[71] We calculated phonon properties using the finite-difference supercell method, perturbing atoms by 0.1 Bohrs to calculate

https://doi.org/10.1021/acs.jpcc.4c02430
J. Phys. Chem. C 2024, 128, 10714−10722

the real space interatomic force constant matrix directly.[72] To improve the accuracy of the phonon modes calculated, we expanded the dynamical matrix by adding submatrices corresponding to the dynamical matrix calculated for Nb bulk. We added enough elements to the matrix to emulate a slab 10 layers deeper than the original one. Interatomic force constant matrices for the slab were evaluated in a 1 × 3 × 1 supercell with a *k*-space sampling density equal to the unit cell's sampling of 3 × 9 × 1 *k*-points. For the Nb bulk, we evaluated in a 4 × 4 × 4 supercell with *k*-space sampling density equal to the unit cell's sampling of the 12 × 12 × 12 *k*-points.

3. RESULTS AND DISCUSSION

The (3 × 1)-O/Nb(100) surface oxide reconstruction was prepared and confirmed with HAS diffraction and AES in Figure 1a,b, respectively. Figure 1a contains a diffraction scan

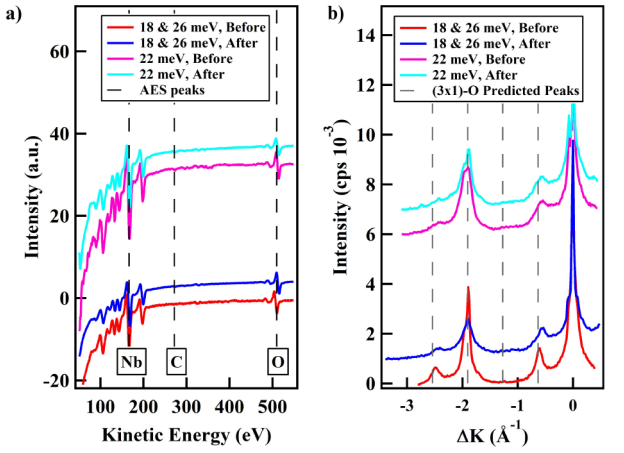

Figure 1. Representative (a) AES adjusted for scale and staggered for visual clarity as well as (b) He atom diffraction spectra along the <$\bar{1}$00> symmetry axis; AES and diffraction spectra were taken before and after the DW measurements on (3 × 1)-O/Nb(100) surface. In panel (a), the primary Nb peak is evident at 167 eV, the secondary Nb peak at 192 eV, and the primary O (503 eV) peak is present in the appropriate range, O/Nb ∼ 0.15−0.3, for the (3 × 1)-O. There is an absence of C (270 eV) and N (379 eV) peaks, indicating a clean Nb surface. In panel (b), there is only the first order diffraction peak. The superlattice peaks of the most likely reconstruction, the oxide reconstruction, lie upon this symmetry direction and are evident.

taken at 550 K along the <$\bar{1}$00>, $\bar{\Gamma}\bar{X}$ azimuthal direction. Each peak occurs when the Von Laue condition holds true, or when

$$\Delta K = k_i(\sin\theta_i - \sin\theta_f) = G_{mn} \quad (1)$$

where the surface-parallel component of the He wavevector k_i changes by ΔK; the initial and final scattering angles, relative to surface normal, are θ_i and θ_f, respectively; and G_{mn} is a linear combination of reciprocal surface lattice vectors.[23,47,51]

Thermal attenuation occurs due to thermally excited phonons disturbing the electron density at the surface. This thermal attenuation is described by the following relation:

$$I(T_S) = I(0)e^{-2W(T_S)} \quad (2)$$

where 2W is the DW factor. The traditional definition of the DW factor is

$$2W(T_S) = \langle \Delta k \cdot u(T_S)\rangle^2 \quad (3)$$

where Δk is the change in wavevector of the scattered He and u is mean squared displacement (MSD) of the surface atoms.[73] Recently, Manson et al. have derived a relationship between 2W and the surface EPC constant via reasonable approximations, yielding the direct proportionality for metal surfaces above the surface Debye temperature,

$$\lambda_{HAS} \cong -\frac{d\ln I_{00}}{k_B dT_S}\frac{\phi}{6Z}\frac{k_F^2}{k_{iz}^2} \quad (4)$$

where I_{00} is the intensity of the specular reflection, ϕ is the work function, Z is the number of free electrons per atom, k_F is the Fermi wavevector, and k_{iz} is the surface perpendicular (z) component of the incident helium incident wavevector.[55,56] In a DW measurement, diffraction scans were taken over the specular peak up and down the temperature range, ∼ 550 to 750 K, for three beam energies (Figure 2). These DW runs were taken immediately following and after confirmation of structure and composition with He diffraction and AES respectively, ensuring cleanliness.

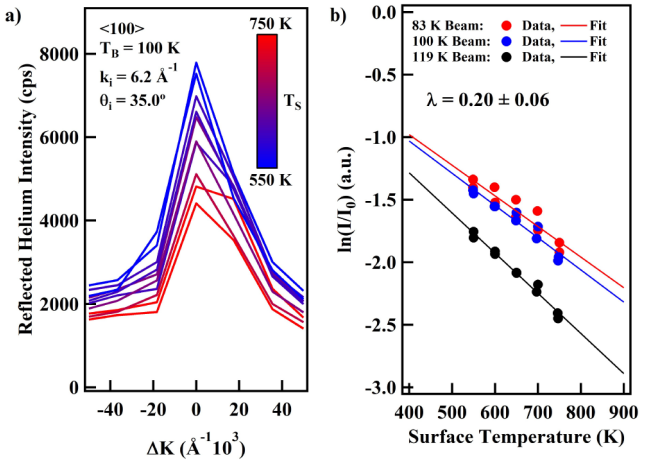

Figure 2. Representative thermal attenuation of the specular peak is observed in (a), where diffraction scans through the range were taken proceeding up the temperature range to 750 K and then back down to 550 K. The intensity values are taken from these specular reflections and plotted in (b). In (b), the ln of specular intensity is plotted versus surface temperature for three beam energies. A linear line is fit to the data, providing I_0 from the y-intercept fitting parameter. I_0 is the specular intensity at 0 K with a perfectly still surface. The fit also provides a slope fitting parameter that is equal to $\frac{d\ln I_{00}}{dT_S}$. From this slope and a work function from UPS, average number of free electrons per atom, and estimated Fermi wavevector, we calculate λ = 0.20 ± 0.06 for the (3 × 1)-O/Nb(100) surface reconstruction.

The beam energies that we used were sufficiently low to require the so-called Beeby correction. The Beeby correction accounts for acceleration due to the attractive portion of the helium-surface potential well depth, D.[74] The Beeby approximation is commonly used to correct for this effect, taking into account the acceleration of the helium atom from the helium surface potential before scattering. In the Beeby approximation, the potential well depth is added to the incident helium beam energy. This quantity can be related to the DW factor by expanding the traditional expression for the DW factor with standard kinematics. Upon substitution, restriction to specular scattering, and rearrangement, the relation,

https://doi.org/10.1021/acs.jpcc.4c02430
J. Phys. Chem. C 2024, 128, 10714−10722

$$\sigma = -\frac{d(2W)}{dT_S} = 4k_i^2 \frac{d\langle u_z^2\rangle}{dT_S}\left[\cos^2\theta_i + \frac{D}{E_i}\right] \quad (5)$$

is obtained, where σ is the negative slope of a DW linear plot, k_i is the helium incident wavevector, θ_i is the incident angle relative to surface normal, D is the helium-surface potential well depth, and E_i is the helium incident energy.[74] Thus, a fit of DW decay, σ, versus $k_i^2 \cos^2\theta_i$ yields the helium-surface potential well depth and the first derivative of the mean-square displacement with respect to surface temperature. These diffraction scans and the corresponding plot of σ versus $k_i^2 \cos^2\theta_i$ are in Figure 3.

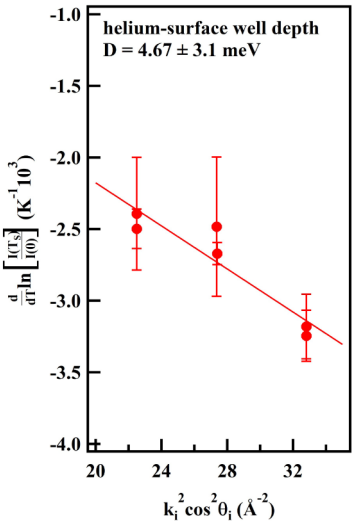

Figure 3. A plot of σ versus $k_i^2 \cos^2\theta_i$ and its fit provides the helium-surface well depth, 4.7 meV, and the surface Debye temperature, 390 ± 10 K. Obtaining a value for the well depth, D, allows us to correct our incident beam energy in the so-called Beeby correction. The surface Debye temperature verifies that the DW measurements were made in the high temperature limit of Bose−Einstein phonon population function required for eq 3 to apply. Additionally, the Debye temperature is used in calculating the T_c from the measured λ in the McMillan equation.

From the fitting parameters, a helium to surface well depth of 4.7 meV was obtained, and a surface Debye temperature of 357 K was determined from the mean squared displacement with the Debye model.

Complementary DFT calculations of phonon modes provided theoretical MSD values. The HAS intensity-vs-temperature data can be converted into MSD_z-vs-temperature data using the traditional definition of the DW factor (eqs 2 and 3) and the Beeby correction to correct the incident He wavevector.[74,75] The excellent agreement between HAS data and the complementary DFT calculations through MSD_z can be seen in Figure 4.

The lines in Figure 4 represent the *apparent* MSD_z calculated with

$$\langle (u_z^2)_a \rangle_T = \frac{1}{p^2}\left\langle \left(\sum_{k=1}^{p} u_z(k)\right)^2 \right\rangle_T \quad (6)$$

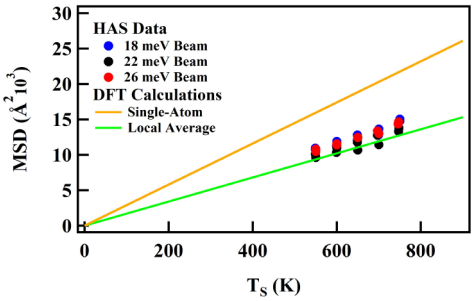

Figure 4. Comparison of HAS data and DFT data via MSD_z (surface perpendicular portion of the MSD). Upper and lower bounds were calculated averaging over single atoms and local averaging in the unit cell, respectively. The local averaging takes the average over nearest and next nearest neighbors. This takes into account the finite volume of the He atom and the fact that it interacts with multiple surface atoms in a single impulsive scattering event. Thus, the apparent MSD_z calculated from local averaging has excellent agreement with the HAS data.

where p is the number of atoms on the surface and $u_z(k)$ is the atomic displacement operator in the normal direction to the surface for the k-th atom, calculated with

$$u_z(\kappa) = \sqrt{\frac{\hbar}{2Nm_\kappa}} \sum_{qj} \frac{\hat{a}_{qj} + \hat{a}^{\dagger}_{-qj}}{\sqrt{\omega_{qj}}} e^{z\kappa}_{qj} e^{iq\cdot r(\kappa)} \quad (7)$$

where the summation samples phonon modes j at wavevectors q throughout the surface's Brillouin zone. $e^{z\kappa}_{qj}$ is the component of the phonon eigenvector corresponding to the normal displacement of the surface atom of mass m_κ, and the Bose factor $n(\omega_{qj}) = a^{\dagger}_{-qj} a_{qj}$ weights the displacements of each sampled phonon mode at temperature T.[51]

Following a similar approach to that used for the metallic, unreconstructed Nb(100) surface,[20] we considered the range of interaction of the electron density of the He atom compared to the electron density of the atoms on the surface, given the distance between them. The upper bound averages over single atoms in the unit cell, considering a shorter interaction range than expected. The lower bound in Figure 4 uses eq 5 to average over nearest and next-to-nearest neighbors, which is often used in the literature.[20,75]

Before we can use the DW slope to calculate λ, we must choose values for the (3 × 1)-O/Nb(100)'s work function, number of free electrons per atom, and Fermi wave vector. The (3 × 1)-O/Nb(100) work function was found to be 4.5 ± 3.8 × 10^{-2} eV and was calculated by subtracting the width of the UPS spectra from the incident photon energy (21.22 eV), as shown in Figure 5. The secondary electron cutoff (SECO) energy was obtained by calibrating the Fermi level using a Au reference sample.[29,76−78]

This fits well with literature that agrees that the work function of Nb, 3.99 eV,[23] generally increases with O impurities and oxide reconstructions, but O can have nonmonotonic effects on the work function.[79,80] The number of free electrons per atom becomes a weighted average between the number of free electrons of Nb and O atoms in the (3 × 1)-O unit cell, yielding 2.7 free electrons per atom. The Fermi wave vector was calculated from the number of free electrons using the free electron model to calculate a Fermi wavevector of 0.89 Å^{-1}.[23] The DW slope and these chosen values of the work function, number of free electrons per atom,

https://doi.org/10.1021/acs.jpcc.4c02430
J. Phys. Chem. C 2024, 128, 10714−10722

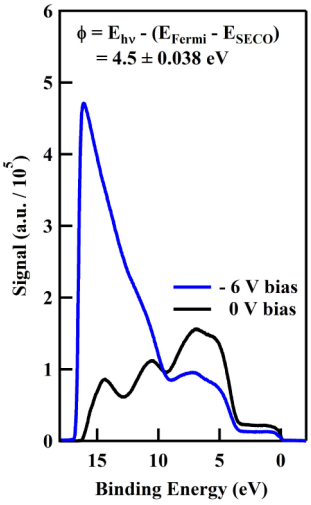

Figure 5. UPS spectra of the (3 × 1)-O/Nb(100) surface using a He I α photon ($E_{h\nu}$: 21.22 eV) with no external bias (black curve) and a −6 V bias (blue curve). The work function was calculated using the inset equation. ESECO of 16.74 eV was found by linearly fitting the SECO x-intercept for the UPS spectrum that was collected with a −6 V bias. The binding energy and Fermi level were calibrated using an Au reference sample. The reported error for the work function was determined by using the energy resolution of the analyzer used in the UPS measurements.

and Fermi wave vector were used to calculate a λ of 0.20 ± 0.06 for the (3 × 1)-O/Nb(100) surface.

This is the first recorded value of λ for the (3 × 1)-O/Nb(100) surface oxide reconstruction. For reference and clarity, the recorded λ values for bulk Nb are 1.15, 1.04, 1.16, and 0.92, almost twice that of the unreconstructed, metallic Nb(100) surface, 0.50 ± 0.08.[20,36−44] While the interface, even without O or reconstruction, diminishes EPC, the (3 × 1)-O reconstruction further diminishes EPC.

Each preparation of the (3 × 1)-O has different amounts of subsurface oxygen. We can make a plot of measured (3 × 1)-O EPC versus AES O content to probe the effect of subsurface oxygen on the (3 × 1)-O reconstruction's EPC (Figure 6).

We find that the amount of subsurface oxygen has no significant effect on the SEPC of the (3 × 1)-O reconstruction. This is distinct from the effect of subsurface oxygen and carbon on the SEPC of the unreconstructed, metallic Nb(100).[20] The

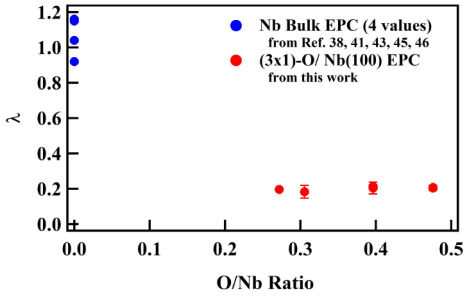

Figure 6. EPC constants were extracted from the DW slopes plotted in Figure 2 (b) and plotted against O/Nb from AES. There is an apparent diminishing of λ_S with varying subsurface O. The amount of subsurface oxygen has no significant effect on the SEPC of the (3 × 1)-O reconstruction. These results show that while the (3 × 1)-O diminishes the SEPC of the metallic, unreconstructed Nb(100) surface, it also stabilizes the SEPC against the effects of subsurface O.

unreconstructed, metallic Nb(100) SEPC had a monotonic decrease with accumulation of subsurface O and C.[20] However, the (3 × 1)-O surface oxide reconstruction is not only robust in terms of its high thermal stability and strong interatomic forces, but also in that its SEPC is not significantly altered by subsurface oxygen.[35,53] These results indicate that even if one removed the problematic oxide[19] within an SRF cavity it would introduce a greater susceptibility to impurities.

To elucidate the significance of the (3 × 1)-O surface oxide reconstruction's diminished λ, we will estimate the critical temperature of this material. In fact, using the Dynes' version of McMillan's equation along with our measured λ and surface Debye temperature as well as the standard range (0.1−0.15) for the renormalized Coulomb repulsion, we find a $T_C \leq 6.2 \times 10^{-4}$ K.[25] We see that the surface oxide reconstruction significantly diminishes T_C to the point that it is not a feasible superconductor on its own. However, the proximity effect occurs when a normal material and superconducting material are in contact with one another.[81−83] Cooper pairs leak into the normal state imparting some superconductivity, while the exodus of Cooper pairs from the superconducting material diminishes its superconducting properties.[84−86] Thus, the (3 × 1)-O/Nb(100) interface will diminish the superconductivity of the underlying bulk Nb while its own superconductivity is increased. Additionally, neither the (3 × 1)-O superlattice nor the HAS probe depth approaches the ∼100 nm RF field penetration depth of Nb SRF cavities.[2,31,55,56] The (3 × 1)-O/Nb(100) does not quench superconductivity but is expected to significantly diminish the overall superconducting performance on the interface and in the underlying, near-surface bulk.

This continues to build a necessary, missing fundamental understanding of the effects of surface structure and composition on EPC and superconducting properties. Now we can begin to understand the changes to the surface caused by carbon impurities, N doping, Sn alloying, and other SRF cavity preparations. These results provide the first measurement of λ of the (3 × 1)-O/Nb(100) surface oxide reconstruction and distinguish the effects of structure and composition of the NbO monolayer surface oxide on the resulting surface superconducting properties.

4. CONCLUSION

The (3 × 1)-O/Nb(100) surface λ_S was measured to be 0.20 ± 0.06 and its atomic-scale surface structure was confirmed, with our findings further supported by consistency between our measured HAS Debye−Waller factors and *ab initio* density-functional theory predictions. The λ_S measured for the (3 × 1)-O surface reconstruction is further diminished from the metallic, unreconstructed Nb(100) value and further from the diminished reported bulk Nb λ values. Furthermore, the amount of subsurface oxygen has no significant effect on the λ_S of the (3 × 1)-O reconstruction. Thus, while the metallic, unreconstructed Nb(100) surface is significantly affected by accumulated C and O, the (3 × 1)-O reconstruction stabilizes its λ_S against the effects of subsurface O. The significance of Nb(100)'s diminished EPC was further elucidated by estimating relevant superconducting properties from the measured λ_S, surface Debye temperature, known material parameters, and well-established equations. Due to the low λ_S, a negligible critical temperature (T_C) $\leq 6.2 \times 10^{-3}$ K was estimated using the McMillan equation. However, this indicates that at operational temperatures of ∼2 K, the (3 × 1)-O/Nb(100) reconstruction is not superconducting on its

https://doi.org/10.1021/acs.jpcc.4c02430
J. Phys. Chem. C 2024, 128, 10714−10722

own. However, the proximity effect indicates that a thin normal metal on top of a superconductor exhibits some superconducting properties while the superconductor's properties are diminished. These results contain the first measurement of (3 × 1)-O/Nb(100) λ_S, distinguish the effects of surface structure and chemical composition on λ_S, and indicate that the (3 × 1)-O/Nb(100) surface has diminished superconducting properties relative to the unreconstructed, metallic Nb(100) and the Nb bulk.

AUTHOR INFORMATION

Corresponding Author

S. J. Sibener − *The James Franck Institute and Department of Chemistry, The University of Chicago, Chicago, Illinois 60637, United States;* orcid.org/0000-0002-5298-5484; Email: s-sibener@uchicago.edu

Authors

Caleb J. Thompson − *The James Franck Institute and Department of Chemistry, The University of Chicago, Chicago, Illinois 60637, United States*

Michael Van Duinen − *The James Franck Institute and Department of Chemistry, The University of Chicago, Chicago, Illinois 60637, United States*

Cristobal Mendez − *Department of Physics, Cornell University, Ithaca, New York 14853, United States;* orcid.org/0000-0002-1257-6707

Sarah A. Willson − *The James Franck Institute and Department of Chemistry, The University of Chicago, Chicago, Illinois 60637, United States*

Van Do − *The James Franck Institute and Department of Chemistry, The University of Chicago, Chicago, Illinois 60637, United States*

Tomás A. Arias − *Department of Physics, Cornell University, Ithaca, New York 14853, United States*

Complete contact information is available at: https://pubs.acs.org/10.1021/acs.jpcc.4c02430

Notes

The authors declare no competing financial interest.

ACKNOWLEDGMENTS

S.J.S. and T.A.A. would like to acknowledge support from the U.S. National Science Foundation under Award PHY-1549132, the Center for Bright Beams, while S.J.S also acknowledges support from the Air Force Office of Scientific Research Grant No. FA9550-19-1-0324 for fundamental studies of gas-surface energy transfer. Support from the NSF-Materials Research Science and Engineering Center at The University of Chicago, Grant No. NSF-DMR-2011854, also is gratefully acknowledged.

REFERENCES

(1) Padamsee, H. The Science and Technology of Superconducting Cavities for Accelerators. *Supercond. Sci. Technol.* **2001**, *14* (4), R28−R51.

(2) Padamsee, H.; Knobloch, J.; Hays, T. RF Superconductivity for Accelerators. In *Wiley Series in Beam Physics and Accelerator Technology*; John Wiley & Sons, Inc.: Cornell University: Ithaca, NY, 1998.

(3) Padamsee, H.; Shepard, K. W.; Sundelin, R. Physics and Accelerator Applications of RF Superconductivity. *Annu. Rev. Nucl. Part. Sci.* **1993**, *43* (1), 635−686.

(4) Posen, S.; Valles, N.; Liepe, M. Radio Frequency Magnetic Field Limits of Nb and Nb 3 Sn. *Phys. Rev. Lett.* **2015**, *115* (4), 047001.

(5) Posen, S. Understanding And Overcoming Limitation Mechanisms In Nb3Sn Superconducting Rf Cavities, Cornell University, 2015. https://ecommons.cornell.edu/handle/1813/39470 (accessed 2022−10−02).

(6) Finnemore, D. K.; Stromberg, T. F.; Swenson, C. A. Superconducting Properties of High-Purity Niobium. *Phys. Rev.* **1966**, *149* (1), 231−243.

(7) Tinkham, M. *Introduction to Superconductivity*; Robert E. Krieger Publishing Company, 1980.

(8) Porter, R.; Banerjee, N.; Liepe, M. Dynamic Temperature Mapping of Nb_3Sn Cavities. *Proceedings Of The 20th International Conference On RF Superconductivity*. JACoW, **2022**, 610. .

(9) Hall, D.; Cueva, P.; Liarte, D.; Liepe, M.; Muller, D.; Porter, R.; Sethna, J. Cavity Quench Studies in Nb3Sn Using Temperature Mapping and Surface Analysis of Cavity Cut-Outs. *Proceedings Of The 18th Int. Conf. On RF Superconductivity* **2018**, 4.

(10) Liarte, D. B.; Posen, S.; Transtrum, M. K.; Catelani, G.; Liepe, M.; Sethna, J. P. Theoretical Estimates of Maximum Fields in Superconducting Resonant Radio Frequency Cavities: Stability Theory, Disorder, and Laminates. *Supercond. Sci. Technol.* **2017**, *30* (3), 033002.

(11) Posen, S.; Hall, D. L. Nb3Sn Superconducting Radiofrequency Cavities: Fabrication, Results, Properties, and Prospects. *Supercond. Sci. Technol.* **2017**, *30* (3), 033004.

(12) Porter, R.; Arias, T.; Cueva, P.; Hall, D.; Liepe, M.; Maniscalco, J.; Muller, D.; Sitaraman, N. *Next Generation Nb3Sn SRF Cavities for Linear Accelerators*; JACOW: Geneva, Switzerland, 2019, pp. 462465. .

(13) Reece, C.; Angle, J.; Kelley, M.; Lechner, E.; Palczewski, A.; Stevie, F. *Challenges to Reliable Production Nitrogen Doping of Nb for SRF Accelerating Cavities*; JACOW: Geneva, Switzerland, 2022, pp. 13111314. .

(14) Ries, R.; Seiler, E.; Gömöry, F.; Medvids, A.; Onufrijevs, P.; Pira, C.; Chyhyrynets, E.; Malyshev, O. B.; Valizadeh, R. Surface Quality Characterization of Thin Nb Films for Superconducting Radiofrequency Cavities. *Supercond. Sci. Technol.* **2022**, *35* (7), 075010.

(15) Checchin, M.; Grassellino, A.; Martinello, M.; Melnychuk, O.; Posen, S.; Romanenko, A.; Sergatskov, D. New Insight on Nitrogen Infusion Revealed by Successive Nanometric Material Removal. *Fermi National Accelerator Lab*; (FNAL), Batavia, IL (United States). 2018, 26652667. .

(16) Grassellino, A.; Romanenko, A.; Sergatskov, D.; Melnychuk, O.; Trenikhina, Y.; Crawford, A.; Rowe, A.; Wong, M.; Khabiboulline, T.; Barkov, F. Nitrogen and Argon Doping of Niobium for Superconducting Radio Frequency Cavities: A Pathway to Highly Efficient Accelerating Structures. *Supercond. Sci. Technol.* **2013**, *26* (10), 102001.

(17) Sitaraman, N. S.; Sun, Z.; Francis, B.; Hire, A. C.; Oseroff, T.; Baraissov, Z.; Arias, T. A.; Hennig, R.; Liepe, M. U.; Muller, D. A.; Transtrum, M. K.. Theory of Nb-Zr Alloy Superconductivity and First Experimental Demonstration for Superconducting Radio-Frequency Cavity Applications; arXiv, 2022. http://arxiv.org/abs/2208.10678 (accessed 2022−10−01).

(18) Ciovati, G.; Myneni, G.; Stevie, F.; Maheshwari, P.; Griffis, D. High Field Q Slope and the Baking Effect: Review of Recent Experimental Results and New Data on Nb Heat Treatments. *Phys. Rev. ST Accel. Beams* **2010**, *13* (2), 022002.

(19) Romanenko, A.; Grassellino, A.; Barkov, F.; Ozelis, J. P. Effect of Mild Baking on Superconducting Niobium Cavities Investigated by Sequential Nanoremoval. *Phys. Rev. ST Accel. Beams* **2013**, *16* (1), 012001.

(20) Thompson, C. J.; Van Duinen, M. F.; Kelley, M. M.; Arias, T. A.; Sibener, S. J. Correlating Electron−Phonon Coupling and In Situ High-Temperature Atomic-Scale Surface Structure at the Metallic Nb(100) Surface by Helium Atom Scattering and Density Functional Theory. *J. Phys. Chem. C* **2024**, *128*, 6149.

(21) Bardeen, J.; Cooper, L. N.; Schrieffer, J. R. Theory of Superconductivity. *Phys. Rev.* **1957**, *108* (5), 1175−1204.
(22) Bardeen, J.; Cooper, L. N.; Schrieffer, J. R. Microscopic Theory of Superconductivity. *Phys. Rev.* **1957**, *106* (1), 162−164.
(23) Ashcroft, N. W.; Mermin, N. D. *Solid State Physics; Brookes/Cole, a part of*; Cengage Learning, 1976.
(24) Grimvall, G. The Electron-Phonon Interaction in Metals*Series of Monographs on Selected Topics in Solid State Physics*North-Holland Publishing Company1981Vol. *16*
(25) Dynes, R. C. McMillan's Equation and the Tc of Superconductors. *Solid State Commun.* **1972**, *10* (7), 615−618.
(26) Farrell, H. H.; Isaacs, H. S.; Strongin, M. The Interaction of Oxygen and Nitrogen with the Niobium (100) Surface: II. Reaction Kinetics. *Surf. Sci.* **1973**, *38* (1), 31−52.
(27) Dawson, P. H.; Tam, W.-C. The Interaction of Oxygen with Polycrystalldve Niobium Studied Using Aes and Low-Energy Sims. *Surf. Sci.* **1979**, *81* (2), 464−478.
(28) Grundner, M.; Halbritter, J. XPS and AES Studies on Oxide Growth and Oxide Coatings on Niobium. *J. Appl. Phys.* **1980**, *51* (1), 397−405.
(29) Hu, Z. P.; Li, Y. P.; Ji, M. R.; Wu, J. X. The Interaction of Oxygen with Niobium Studied by XPS and UPS. *Solid State Commun.* **1989**, *71* (10), 849−852.
(30) Rieder, K. H. On the Interaction of Oxygen with Nb(110) and Nb(750). *Appl. Surf. Sci.* **1980**, *4* (2), 183−195.
(31) An, B.; Fukuyama, S.; Yokogawa, K.; Yoshimura, M. Surface Structures of Clean and Oxidized Nb(100) by LEED, AES, and STM. *Phys. Rev. B* **2003**, *68* (11), 115423.
(32) Veit, R. D.; Kautz, N. A.; Farber, R. G.; Sibener, S. J. Oxygen Dissolution and Surface Oxide Reconstructions on Nb(100). *Surf. Sci.* **2019**, *688*, 63−68.
(33) Lindau, I.; Spicer, W. E. Oxidation of Nb as Studied by the Uv-photoemission Technique. *J. Appl. Phys.* **1974**, *45* (9), 3720−3725.
(34) Arfaoui, I.; Cousty, J.; Guillot, C. A Model of the NbOx≈1 Nanocrystals Tiling a Nb(110) Surface Annealed in UHV. *Surf. Sci.* **2004**, *557* (1), 119−128.
(35) McMillan, A. A.; Graham, J. D.; Willson, S. A.; Farber, R. G.; Thompson, C. J.; Sibener, S. J. Persistence of the Nb(100) Surface Oxide Reconstruction at Elevated Temperatures. *Supercond. Sci. Technol.* **2020**, *33* (10), 105012.
(36) Butler, W. H.; Smith, H. G.; Wakabayashi, N. Electron-Phonon Contribution to the Phonon Linewidth in Nb: Theory and Experiment. *Phys. Rev. Lett* **1977**, *39* (16), 1004−1007.
(37) Shapiro, S. M.; Shirane, G.; Axe, J. D. Measurements of the Electron-Phonon Interaction in Nb by Inelastic Neutron Scattering. *Phys. Rev. B* **1975**, *12* (11), 4899−4908.
(38) DeSorbo, W. Effect of Dissolved Gases on Some Superconducting Properties of Niobium. *Phys. Rev.* **1963**, *132* (1), 107−121.
(39) Koch, C. C.; Scarbrough, J. O.; Kroeger, D. M. Effects of Interstitial Oxygen on the Superconductivity of Niobium. *Phys. Rev. B* **1974**, *9* (3), 888−897.
(40) Gupta, M. Electronic Properties and Electron-Phonon Coupling in Zirconium and Niobium Hydrides. *Phys. Rev. B* **1982**, *25* (2), 1027−1038.
(41) Ponosov, Y. S.; Streltsov, S. V. Measurements of Raman Scattering by Electrons in Metals: The Effects of Electron-Phonon Coupling. *Phys. Rev. B* **2012**, *86* (4), 045138.
(42) Aynajian, P.; Keller, T.; Boeri, L.; Shapiro, S. M.; Habicht, K.; Keimer, B. Energy Gaps and Kohn Anomalies in Elemental Superconductors. *Science* **2008**, *319* (5869), 1509−1512.
(43) Brorson, S. D.; Kazeroonian, A.; Moodera, J. S.; Face, D. W.; Cheng, T. K.; Ippen, E. P.; Dresselhaus, M. S.; Dresselhaus, G. Femtosecond Room-Temperature Measurement of the Electron-Phonon Coupling Constant γ in Metallic Superconductors. *Phys. Rev. Lett.* **1990**, *64* (18), 2172−2175.
(44) Bennemann, K. H.; Garland, J. W.; Wolfe, H. C.; Douglass, D. H.; *Theory for Superconductivity in D-Band Metals*; Rochester, New York, USA: 1972pp. 103137. DOI:.
(45) Arnold, G. B.; Zasadzinski, J.; Osmun, J. W.; Wolf, E. L. Proximity Electron Tunneling Spectroscopy. II. Effects of the Induced N-Metal Pair Potential on Calculated S-Metal Properties. *J. Low Temp. Phys.* **1980**, *40* (3), 225−246.
(46) Wolf, E. L.; Zasadzinski, J.; Osmun, J. W.; Arnold, G. B. Proximity Electron Tunneling Spectroscopy I. Experiments on Nb. *J. Low Temp. Phys.* **1980**, *40* (1), 19−50.
(47) Scoles, G.; Bassi, D.; Buck, U.; Laine, D. *Atomic and Molecular Beam Methods*; Oxford University Press, 1988; Vol. *1*.
(48) Scoles, G.; Laine, D.; Valbusa, U. *Atomic and Molecular Beam Methods*; Oxford University Press, 1992; Vol. *2*.
(49) Estermann, I.; Stern, O. B. V. M. Beugung von Molekularstrahlen. *Z. Physik* **1930**, *61* (1), 95−125.
(50) *Helium Atom Scattering from Surfaces*Hulpke, E.Springer-VerlagBerlin1992Vol. *27*
(51) Benedek, G.; Toennies, J. P. *Atomic Scale Dynamics at Surfaces: Theory and Experimental Studies with Helium Atom Scattering*; Springer: Berlin, Heidelberg, 2018; Vol. *63*. .
(52) Kress, W.; de Wette, F. W. *Surface Phonons*; Springer-Verlag: Berlin, 1991.
(53) McMillan, A. A.; Thompson, C. J.; Kelley, M. M.; Graham, J. D.; Arias, T. A.; Sibener, S. J. A Combined Helium Atom Scattering and Density-Functional Theory Study of the Nb(100) Surface Oxide Reconstruction: Phonon Band Structures and Vibrational Dynamics. *J. Chem. Phys.* **2022**, *156* (12), 124702.
(54) Esbjerg, N.; Nørskov, J. K. Dependence of the He-Scattering Potential at Surfaces on the Surface-Electron-Density Profile. *Phys. Rev. Lett.* **1980**, *45* (10), 807−810.
(55) Manson, J. R.; Benedek, G.; Miret-Artés, S. Electron−Phonon Coupling Strength at Metal Surfaces Directly Determined from the Helium Atom Scattering Debye−Waller Factor. *J. Phys. Chem. Lett.* **2016**, *7* (6), 1016−1021.
(56) Manson, J. R.; Benedek, G.; Miret-Artés, S. Correction to "Electron−Phonon Coupling Strength at Metal Surfaces Directly Determined from the Helium Atom Scattering Debye−Waller Factor. *J. Phys. Chem. Lett.* **2016**, *7* (9), 1691−1691.
(57) Holst, B.; Alexandrowicz, G.; Avidor, N.; Benedek, G.; Bracco, G.; E. Ernst, W.; Farífarías, D.; P. Jardine, A.; Lefmann, K.; R. Manson, J.; et al. Material Properties Particularly Suited to Be Measured with Helium Scattering: Selected Examples from 2D Materials, van Der Waals Heterostructures, Glassy Materials, Catalytic Substrates, Topological Insulators and Superconducting Radio Frequency Materials. *Phys. Chem. Chem. Phys.* **2021**, *23* (13), 7653−7672.
(58) Luo, N. S.; Ruggerone, P.; Toennies, J. P.; Benedek, G. Electron-Phonon Coupling at Metal Surfaces Probed by Helium Atom Scattering. *Phys. Scr.* **1993**, *T49B*, 584−592.
(59) Benedek, G.; Miret-Artés, S.; Manson, J. R.; Ruckhofer, A.; Ernst, W. E.; Tamtögl, A. Origin of the Electron−Phonon Interaction of Topological Semimetal Surfaces Measured with Helium Atom Scattering. *J. Phys. Chem. Lett.* **2020**, *11* (5), 1927−1933.
(60) Tamtögl, A.; Kraus, P.; Avidor, N.; Bremholm, M.; Hedegaard, E. M. J.; Iversen, B. B.; Bianchi, M.; Hofmann, P.; Ellis, J.; Allison, W.; Benedek, G.; Ernst, W. E. Electron-Phonon Coupling and Surface Debye Temperature of Bi 2 Te 3 (111) from Helium Atom Scattering. *Phys. Rev. B* **2017**, *95* (19), 195401.
(61) Anemone, G.; Taleb, A. A.; Benedek, G.; Castellanos-Gomez, A.; Farífarías, D. Electron−Phonon Coupling Constant of 2H-MoS2(0001) from Helium-Atom Scattering. *J. Phys. Chem. C* **2019**, *123* (6), 3682−3686.
(62) Benedek, G.; Manson, J. R.; Miret-Artés, S. The Electron−Phonon Coupling Constant for Single-Layer Graphene on Metal Substrates Determined from He Atom Scattering. *Phys. Chem. Chem. Phys.* **2021**, *23* (13), 7575−7585.
(63) Benedek, G.; Manson, J. R.; Miret-Artés, S. The Electron−Phonon Interaction of Low-Dimensional and Multi-Dimensional Materials from He Atom Scattering. *Adv. Mater.* **2020**, *32* (25), 2002072.

(64) Benedek, G.; Miret-Artés, S.; Toennies, J. P.; Manson, J. R. Electron−Phonon Coupling Constant of Metallic Overlayers from Specular He Atom Scattering. *J. Phys. Chem. Lett.* **2018**, *9* (1), 76−83.
(65) Gans, B.; Knipp, P. A.; Koleske, D. D.; Sibener, S. J. Surface Dynamics of Ordered Cu3Au(001) Studied by Elastic and Inelastic Helium Atom Scattering. *Surf. Sci.* **1992**, *264* (1), 81−94.
(66) Niu, L.; Gaspar, D. J.; Sibener, S. J. Phonons Localized at Step Edges: A Route to Understanding Forces at Extended Surface Defects. *Science* **1995**, *268* (5212), 847−850.
(67) Payne, M. C.; Teter, M. P.; Allan, D. C.; Arias, T. A.; Joannopoulos, J. D. Iterative Minimization Techniques for Ab Initio Total-Energy Calculations: Molecular Dynamics and Conjugate Gradients. *Rev. Mod. Phys.* **1992**, *64* (4), 1045−1097.
(68) Sundararaman, R.; Letchworth-Weaver, K.; Schwarz, K. A.; Gunceler, D.; Ozhabes, Y.; Arias, T. A. JDFTx: Software for Joint Density-Functional Theory. *SoftwareX* **2017**, *6*, 278−284.
(69) Garrity, K. F.; Bennett, J. W.; Rabe, K. M.; Vanderbilt, D. Pseudopotentials for High-Throughput DFT Calculations. *Comput. Mater. Sci.* **2014**, *81*, 446−452.
(70) Perdew, J. P.; Ruzsinszky, A.; Csonka, G. I.; Vydrov, O. A.; Scuseria, G. E.; Constantin, L. A.; Zhou, X.; Burke, K. Restoring the Density-Gradient Expansion for Exchange in Solids and Surfaces. *Phys. Rev. Lett.* **2008**, *100* (13), 136406.
(71) Sundararaman, R.; Arias, T. A. Regularization of the Coulomb Singularity in Exact Exchange by Wigner-Seitz Truncated Interactions: Towards Chemical Accuracy in Nontrivial Systems. *Phys. Rev. B* **2013**, *87* (16), 165122.
(72) Brown, A. M.; Sundararaman, R.; Narang, P.; Goddard, W. A.; Atwater, H. A. Nonradiative Plasmon Decay and Hot Carrier Dynamics: Effects of Phonons, Surfaces, and Geometry. *ACS Nano* **2016**, *10* (1), 957−966.
(73) Levi, A. C.; Suhl, H. Quantum Theory of Atom-Surface Scattering: Debye-Waller Factor. *Surf. Sci.* **1979**, *88* (1), 221−254.
(74) Beeby, J. L. The Scattering of Helium Atoms from Surfaces. *J. Phys. C: Solid State Phys.* **1971**, *4* (18), L359.
(75) Armand, G.; Lapujoulade, J.; Lejay, Y. The Debye-Waller Factor in Helium Scattering by a Crystalline Surface. *Surf. Sci.* **1977**, *63*, 143−152.
(76) Kim, J. W.; Kim, A. Absolute Work Function Measurement by Using Photoelectron Spectroscopy. *Curr. Appl. Phys.* **2021**, *31*, 52−59.
(77) Erbudak, M.; Gubanov, V. A.; Kurmaev, E. Z. The Electronic Structure of NbO: Theory and Experiment. *J. Phys. Chem. Solids* **1978**, *39* (11), 1157−1161.
(78) Lo, W.-S.; Chen, H.-H.; Chien, T.-S.; Tsan, C.-C.; Fang, B.-S. OXIDATION OF Nb(001) STUDIED BY HIGH-RESOLUTION CORE-LEVEL PHOTOEMISSION. *Surf. Rev. Lett.* **1997**, *04* (4), 651−654.
(79) Wu, A.; Chen, L.; Chu, Q.; Guo, H.; He, Y.; Li, Y.; Pan, F.; Yang, L.; Zhang, S.; Zhao, H. Investigation on Depth Profiling of Niobium Surface Composition and Work Function of SRF Cavities. *Proceedings Of The 18th Int. Conf. On RF Superconductivity* **2018**, 4.
(80) Daccà, A.; Gemme, G.; Mattera, L.; Parodi, R. XPS Analysis of the Surface Composition of Niobium for Superconducting RF Cavities. *Appl. Surf. Sci.* **1998**, *126* (3), 219−230.
(81) Kircher, C. J. Superconducting Proximity Effect of Nb. *Phys. Rev.* **1968**, *168* (2), 437−441.
(82) Kim, J.; Doh, Y.-J.; Char, K.; Doh, H.; Choi, H.-Y. Proximity Effect in Nb / Au / Co Fe Trilayers. *Phys. Rev. B* **2005**, *71* (21), 214519.
(83) Chiodi, F.; Duvauchelle, J.-E.; Marcenat, C.; Débarre, D.; Lefloch, F. Proximity-Induced Superconductivity in All-Silicon Superconductor /Normal-Metal Junctions. *Phys. Rev. B* **2017**, *96* (2), 024503.
(84) Gurevich, A.; Kubo, T. Surface Impedance and Optimum Surface Resistance of a Superconductor with an Imperfect Surface. *Phys. Rev. B* **2017**, *96* (18), 184515.
(85) Belzig, W.; Wilhelm, F. K.; Bruder, C.; Schön, G.; Zaikin, A. D. Quasiclassical Green's Function Approach to Mesoscopic Superconductivity. *Superlattices Microstruct.* **1999**, *25* (5−6), 1251−1288.
(86) Nambu, Y. Quasi-Particles and Gauge Invariance in the Theory of Superconductivity. *Phys. Rev.* **1960**, *117* (3), 648−663.

https://doi.org/10.1021/acs.jpcc.4c02430
J. Phys. Chem. C 2024, 128, 10714−10722